APPLIED SCIENCES AND ENGINEERING

Hidden-information extraction from layered structures through terahertz imaging down to ultralow SNR

Yuqing Cui[1], Yafei Xu[1], Donghai Han[1], Xingyu Wang[1], Zhonglei Shen[1], Yushan Hou[1], Junyan Liang[2], Xianqiao Wang[3], David S. Citrin[4,5], Liuyang Zhang[1]*, Asoke K. Nandi[1,6], Ruqiang Yan[1], Xuefeng Chen[1]

Noninvasive inspection of layered structures has remained a long-standing challenge for time-resolved imaging techniques, where both resolution and contrast are compromised by prominent signal attenuation, interlayer reflections, and dispersion. Our method based on terahertz (THz) time-domain spectroscopy overcomes these limitations by offering fine resolution and a broadband spectrum to efficiently extract hidden structural and content information from layered structures. We exploit local symmetrical characteristics of reflected THz pulses to determine the location of each layer, and apply a statistical process in the spatiotemporal domain to enhance the image contrast. Its superior performance is evidenced by the extraction of alphabetic characters in 26-layer subwavelength papers as well as layer reconstruction and debonding inspection in the conservation of Terra-Cotta Warriors. Our method enables accurate structure reconstruction and high-contrast imaging of layered structures at ultralow signal-to-noise ratio, which holds great potential for internal inspection of cultural artifacts, electronic components, coatings, and composites with dozens of submillimeter layers.

INTRODUCTION

Imaging in the terahertz band (0.1 to 10 THz, equivalent to 3 mm to 30 μm in wavelength) has seen great growth in interest in recent years due to its nonionizing nature as well as the high degree of transparency in this spectral regime in many nonpolar dielectrics (*1*–*3*). Terahertz time-domain spectroscopy (THz-TDS) has become a leading nondestructive spectroscopic testing and 3D imaging technique for determining the properties of a sample probed by short pulses of THz electromagnetic radiation (*4*, *5*). Compared with x-ray tomography, optical coherent tomography, and ultrasonic techniques, THz-TDS provides both fine resolution (*6*) and broadband spectral signature (*7*) that can be used in the inspection of layered structures such as cultural artifacts (*8*, *9*), pharmaceutical tablets (*10*, *11*), coatings (*12*, *13*), as well as composite structures (*14*–*16*).

Despite these advantages, THz-TDS still faces several challenges for broad practical implementation. The submilliwatt power of THz-TDS sources is too feeble to penetrate deeply layered material for information extraction (*17*). The signal-to-noise ratio (SNR) drops markedly in the wave-propagation pathway due to reflections, scattering, and absorption. Moreover, multiple reflections generate numerous small pulses and result in notable oscillations in the THz time-domain signal, making it rather difficult to determine the accurate position and amplitude of THz pulses (*18*). Other factors such as layer distortion and nonlinear zero drift further decrease the contrast and consistency of THz images (*19*), in some cases rendering key information unrecognizable. In addition, when the layer thicknesses are insufficiently large, temporal overlap of pulses reflected off adjacent interfaces takes place among deep layers due to some serious dispersion (*20*). In THz imaging, those regions with lower transmissivity in overlying layers cast shadows on those below that can lead to artifacts in transverse imaging of deeper-lying layers (*21*). Tremendous efforts have been devoted for SNR enhancement with wavelet-based (*22*) or frequency-domain (*18*) methods, but these methods fail in structures with more than a dozen layers due to nonlinear changes of frequency spectrum by out-of-focus and multiple reflections. Attempts have also been made to improve the image contrast and consistency under layer distortion using optimization techniques (*19*, *23*). However, such techniques typically rely on the expectation that the detected THz signals strictly follow the given model, which may no longer be valid in the presence of severe noise. Sparse-representation methods have been introduced into THz imaging to deal with severe pulse overlap (*24*), but the actual detected signal may lose sparsity because of multiple reflections in deep layers. In summary, THz inspection through dozens of layers remains a great challenge despite its attractive features for various applications.

In this work, we propose a locating and imaging technique for hidden-information extraction from layered structures in the case of ultralow SNR. Our method uses the local symmetrical characteristics of the THz signal and peak point cloud density to reconstruct the stratigraphy of layered structures and uses a statistical process in the spatiotemporal domain to enhance the image contrast and to eliminate unwanted image superpositions. To demonstrate the approach to enable both stratigraphic reconstruction and imaging within individual layers, we have successfully extracted hidden alphabetic characters from a layered paper stack and have accomplished the layer reconstruction and debonding inspection in the conservation of Terra-Cotta Warriors. This approach provides an innovative inspection technique with high image contrast and profound penetration depth for layered structures prevalent in the industrial scenario and holds potential for other pulse imaging fields.

[1]State Key Laboratory for Manufacturing Systems Engineering, Xi'an Jiaotong University, Xi'an, Shaanxi 710049, People's Republic of China. [2]School of Chemistry, Xi'an Jiaotong University, Xi'an, Shaanxi 710049, People's Republic of China. [3]School of ECAM, University of Georgia, Athens, GA 30602, USA. [4]School of Electrical and Computer Engineering, Georgia Institute of Technology, Atlanta, GA 30332, USA. [5]Georgia Tech-CNRS IRL2958, Georgia Tech Lorraine, 2 Rue Marconi, 57070 Metz, France. [6]Department of Electronic and Electrical Engineering, Brunel University London, Uxbridge UB8 3PH, UK.
*Corresponding author. Email: liuyangzhang@xjtu.edu.cn

RESULTS

Measurement setup and processing framework

Figure 1 schematically shows the overall measurement setup and processing framework in the experiment and analysis. A pair of photoconductive antennas is set in a reflection geometry to measure a 30-layer stack of paper written with alphabetic letters, as shown in Fig. 1. The centers of these letters are not aligned along the z axis. By taking the surface roughness of the paper sheets into account, there exists a thin air gap between any two adjacent paper sheets, and this gap can act as an interface. The emitted THz pulse through the lens gets concentrated on the sample, while the reflected THz signal is composed of a sequence of pulses originating at the various interfaces. THz-TDS captures the reflected THz signal and provides both the time-of-flight and reflectivity information of the sample.

Signal analysis and physical explanation

Figure 2A shows a measured THz time-domain signal of the 30-layer paper stack in Fig. 1. The measured signal raises three major challenges for the information extraction, including severe signal attenuation and drift, notable oscillations, as well as prominent pulse overlap and shadows. First, it can be observed that signal amplitudes of even the first few layers are ~3.5% that of the incident reference signal produced by our apparatus (red line in inset plot), whereas the last several pulses barely discernable become submerged in noise. The signal attenuation is mainly attributed to the confocal setup of the instrument, water-vapor absorption, and transmission losses in the paper stack. Meanwhile, despite the zero-mean oscillatory nature of THz waves, the zero drift of the instrument causes a nonlinear change in the center of signal oscillation. This zero drift, which is of the same order of magnitude as THz pulses, imposes additional challenges to identifying the pulse profile.

Second, notable oscillation rises from the middle part of the reflected signal as the penetration depth increases. As shown in Fig. 2B, the layered sample can be viewed as a structure composed of odd-indexed layers with refractive index n_1 and even-indexed layers with refractive index n_2 all with equal layer thickness d. The transmissivity and reflectivity of each interface are defined as τ and ρ, respectively. For normal incident waves, $\rho = \left(\frac{n_1-n_2}{n_1+n_2}\right)^2$ and $\tau = 1 - \rho$. Thus, reflected signal $s(t)$ can be expressed as the convolution of the reference pulse $s_{\mathrm{ref}}(t)$ with the reflection impulse response $r(t)$ $s(t) = s_{\mathrm{ref}}(t) * r(t)$ (*19*). Similar to single dielectric slab (*25*), the reflection impulse response contains a series of impulse functions with amplitude u_i being exponential to the number of transmissions and reflections while the delay time t_i is proportional to the optical path length, $r(t) = \sum u_i \delta(t_i)$, where δ represents unit impulse function.

As shown in Fig. 2B, there are numerous feasible propagation paths corresponding to the terms in the reflection impulse response. The left propagation path is the single reflection from the interface between the sixth and seventh layers, which is generally considered to be the seventh pulse in the reflected THz signal. The middle and right propagation paths are examples of multiple reflections with the same propagation length as the left one. These multiple reflections also generate pulses in the reflected THz signal, which can be analyzed by calculating the reflection impulse response. For THz waves that propagate through $2m$ layers and are reflected $(2k + 1)$ times $(m \geq k + 1, k \geq 0)$, the total number of all feasible propagation paths can be described as $q(m,k) = \frac{m-k}{m(k+1)}\left(C_m^k\right)^2$, where C is the symbol of combinatorial number (see section S1 for details). For

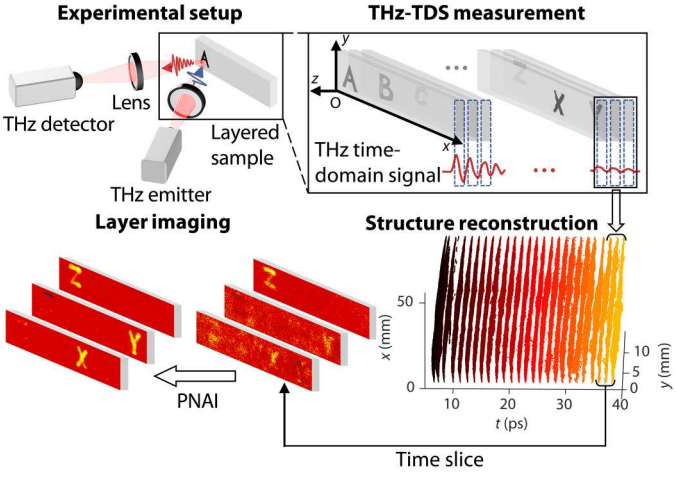

Fig. 1. Schematic diagram of information extraction process via THz imaging. The measurement is conducted by THz-TDS in the reflection mode for raster scan. The reflected signal composed of dozens of pulses provides both time-of-flight and reflectivity information of the sample, which can be used for subsequent stratigraphic reconstruction and transverse imaging within individual layers.

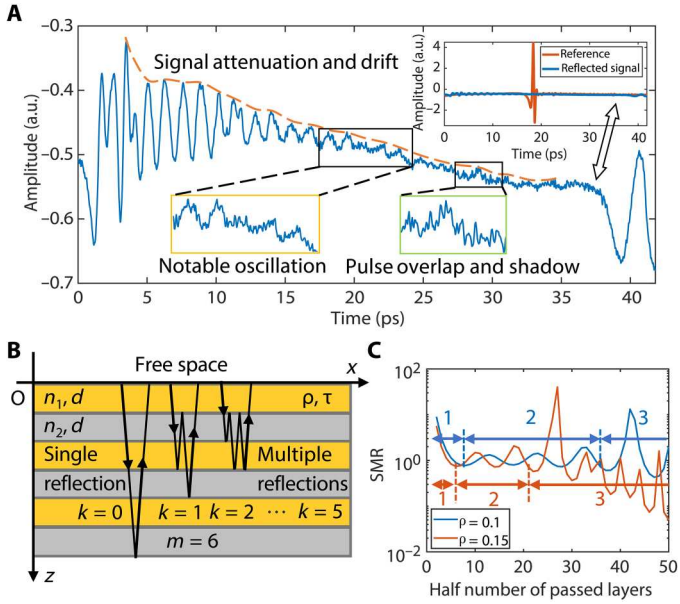

Fig. 2. Signal analysis and reflection model. (**A**) Example of a THz time-domain signal reflected from the layered sample. The vertical axis indicates the amplitude of the reflected electric field in arbitrary units (a.u.), and the horizontal axis represents the time of flight. The orange dashed line indicates the signal envelope. The inset figure shows a comparison between the reference and reflected signals illustrating how weak the latter is by comparison with the former. The peak-to-peak value of the reference pulse is 7.6. (**B**) Reflection model in periodic dielectric layered stack. Yellow and brown indicate odd-indexed and even-indexed layers, respectively. Black arrows represent some possible paths for THz waves passing through 12 layers ($m = 6$). (**C**) The ratio of single- to multiple-reflection amplitudes under various reflectivity ρ.

each feasible propagation path, the amplitude of the impulse function can be expressed by $u(m,k) = (-1)^{m+k+1}\rho^{k+\frac{1}{2}}\tau^{m-k}$. The amplitude would be negative when $(m + k)$ is even due to the existence of half-wave loss. For all propagation paths with the same m, the delay time is almost equal when n_1 is approximately equal to n_2, and therefore the reflection impulse response of these paths can be determined by $r_m = \sum_{k=0}^{m-1} q(m,k)u(m,k)\delta\left(\frac{2mn_1d}{c}\right)$, where $k = 0$ represents single reflection and $k \geq 1$ represents multiple reflections.

Theoretically, the impulse response amplitude $u(m,k)$ decays exponentially with increasing k when $\tau \gg \rho$. Therefore, previous studies usually simplified the reflected THz signal into the pulse sequence of single reflections without involving the effect of complex multiple reflections (*18*). However, this simplified assumption is not sufficient for structures with dozens of layers as the total number of propagation paths q can be extremely large with the increasing layer number. To demonstrate the impact of multiple reflections, Fig. 2C shows the single-reflection amplitude to multiple-reflection amplitude ratio (SMR) under various half number of passed layers m. For a single reflection, m represents the index of interfaces at which the reflection occurs. SMR exhibits three distinct stages as m is increased: a smooth descent stage, an oscillating stage, and an oscillating descent stage. Small reflectivity ρ leads to a large SMR in the first stage, while SMR oscillates around 1 in the second stage regardless of the reflectivity. This can be explained by the counteractive effect of multiple reflections as half-wave loss alternates with k for the same m. Following the oscillating stage, SMR continues to decrease with prominent oscillations, possibly reaching the limit of the number of layers that can be detected by reflected pulse imaging techniques. In addition, because of the random deviation of the layer thicknesses of practical samples, the delay times t_i of the single-reflection and multiple-reflection pulses are not exactly equal even for the same m, which means that complex pulses caused by multiple reflections are scattered around a single-reflection pulse. These randomly distributed tiny pulses cause noticeable oscillation in the THz signal to change the pulse shape and can be considered as stochastic noise (zoomed view in the yellow box in Fig. 2A). Therefore, the noise induced by irregular multiple reflections would exceed single-reflection signal in deep layers and causes notable oscillation in the reflected signal, which will emerge extra challenges for THz signal analysis and feature extraction.

Third, as each layer has a similar optical thickness, the reflected signal consists of evenly spaced pulses. When the pulse width is not sufficiently small compared to the optical path of one round trip through a layer $2nd/c$, prominent overlap of reflected pulses from adjacent layers occurs, leading to a change in the pulse amplitudes. Overlap, moreover, inevitably occurs in deep-layered structures due to serious wave dispersion. In addition, when the THz plane wave incidents into the planar slab with different reflectivities at different positions, the wave amplitude is encoded with the transmissivity information about the slab. Regions with low transmissivity on the slab can generate undesired shadows in the THz images of a few subsequent layers, which degrades the image quality and hinders feature discrimination. As shown in Fig. 2A, a strong reflected pulse of the character (zoomed view in the green box) overlaps with adjacent pulses reflected from blank areas and decreases the energy of the transmitted THz wave, which reduces the pulse amplitude reflected off subsequent layers. Therefore, pulse overlap and shadow exert special disturbance by mixing the contents between different layers.

Layer-structure reconstruction

For layered samples tested by THz-TDS, pulse position is generally used to reconstruct layer structure and to determine the appropriate time slice for transverse imaging in the respective layer. The appropriate extraction of pulse position partially determines the image quality. On account of the complexity of THz signals reflected from structures with dozens of layers, deconvolution techniques that have hitherto attracted the attention of the THz community might be compromised because of serious pulse distortion resulting from multiple reflections and dispersion. Time-domain features such as pulse amplitude and derivative are susceptible to multiple-reflection-induced oscillation and zero drift, leading to poor performance in deep layers when the SNR is below one. The previous work has demonstrated that a double Gaussian mixture model can be used to model the bipolar THz pulse (*20*), and thus, the reflected THz signal can be reasonably modeled as a series of Gaussian pulses. As long as pulse overlap is not severe, every single Gaussian pulse can be considered to be symmetrical around its central peak.

On the basis of the local symmetry in the THz pulse sequence, we develop a pulse position extraction algorithm, namely, local symmetry peak finding (LSPF) (see sections S2 and S3 for details). Local symmetry can be quantified by a local symmetry function (LSF), which compares the left side with the right side of the neighborhood point-by-point. For actual THz pulse sequences, peak points have excellent local symmetry and appear as local minima in LSF. At the rising and falling edge of THz pulses, the signal shows the least local symmetry, and LSF reaches its local maxima. Thus, time-domain peaks correspond to the local minima located between two local maxima in the LSF. This provides a critical threshold to identify authentic peaks and ensures the sparsity of extracted peaks. Detailed procedure of the LSPF algorithm can be found in section S2 and algorithm S1 in the supplementary material.

Figure 3 shows the compared results among different pulse extraction techniques on the measured THz signals from layered samples. Canny edge detection (*26*) and probabilistic pulse extraction (PPEX) (*18*) only detect two-thirds of the pages and fail in the last dozen layers (Fig. 3, B and C). This can be explained that in deep layers, SNR quickly drops below one and the recorded signal is dominated by noise. Meanwhile, multiple-reflection-induced oscillation serves as high-frequency noise to markedly modulate the derivatives of the signal. Besides, nonlinear zero drift makes it difficult to calculate the accurate pulse amplitude. Therefore, common features such as pulse shape, amplitude, and derivative are no longer suitable for layered structures with low SNR.

Figure 3D also shows that LSPF has successfully extracted up to 28 layers with high accuracy, with the last two sheets overshadowed by intense broadened pulses reflected off the bottom metal sheet. Compared with other time-domain peak finding techniques, LSPF captures symmetrical features of THz pulses that are nearly invariant under dispersion and oscillation. The point-by-point comparison process in LSF not only suppresses high-frequency components induced by multiple reflections and stochastic noise but also eliminates the negative effect of zero drift. In addition, conventional methods such as PPEX expect THz pulses with similar

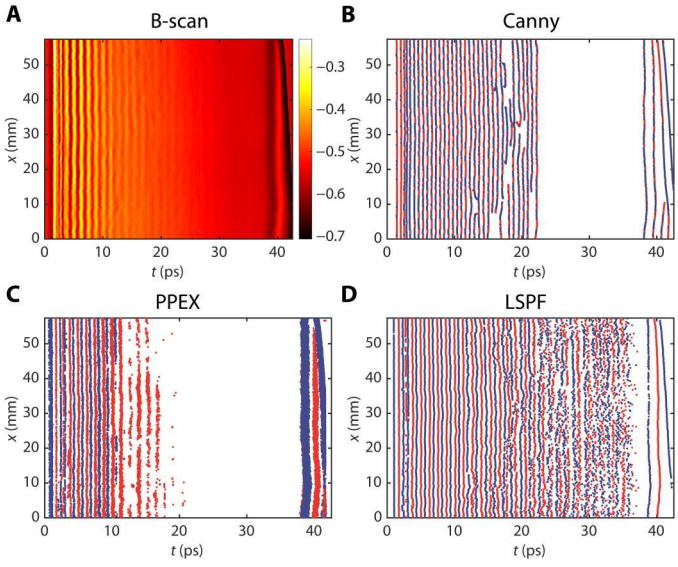

Fig. 3. Comparison of pulse extraction ability of Canny, PPEX, and LSPF methods. (**A**) B-scan of measured data at y = 1.25 mm. The first pulses of different signals are aligned to the same delay time. Image intensity indicates signal amplitude in arbitrary units. (**B**) Canny edge detection. (**C**) PPEX. (**D**) LSPF. Blue points indicate that the THz time-domain signal amplitude is smaller than that nearby, and red points indicate that the signal amplitude is greater. The rightmost points represent strong reflections from the bottom metal sheet.

SNR for appropriate filtering and processing, while weak pulses may be completely neglected. By contrast, LSF acts as a standardization process to improve the consistency under different SNRs. This is particularly critical because actual THz signals often consist of many pulses subject to various noise levels. Moreover, LSPF does not require the reference signal, and its computation speed would be even faster than PPEX with a wavelet filter. Comparison of the peak finding methods from the simulation perspective can be found in section S4.

As a peak finding method, LSPF only extracts peak positions to generate a peak point cloud without identifying the interface to which they belong, and thus, layer segmentation is necessary to group the peak point cloud corresponding to the layers. For flat layers with uniform thickness, cloud segmentation can be commonly tackled by one-dimensional clustering. However, for structures with dozens of layers, peak points are gradually scattered around the actual interface as the peak finding accuracy degrades with the depth, and layers are usually slightly distorted despite the alignment. Thus, when the layer thickness is insufficiently large, peak points from different interfaces will mix to a large degree, which results in catastrophic failure and complete loss of layer information by traditional clustering algorithms. Therefore, we propose a local minimum density segmentation (LMDS) algorithm based on the periodic change of point cloud density (see section S5 for details).

In the peak finding process, peak positioning error is tightly determined by the SNR of the THz signal and can be considered to follow a Gaussian distribution as well. Consequently, the point cloud tends to be of high density as peak points are more likely to be distributed near the real interface. The common definition of point cloud density counts the number of points in a certain interval as $d_0(t) = \frac{1}{2\alpha}\sum_{i=1}^{n} u(\alpha - t + p_i)u(\alpha + t - p_i)$, where u is the unit step function, p_i represents the point position in the peak point cloud, n is the total number of points, and α is the interval length. The sharp rectangular window composed of step functions can be replaced by a Gaussian window $d(t) = \sum_{i=1}^{n} e^{-(t-p_i)^2}$ to improve the smoothness of the density function. From the redefined density function, local maxima represent the interfaces while local minima represent the segmentation boundary. The local mode of local minima is calculated subsequently to extract the boundaries, and all the points between two adjacent boundaries will be labeled as the same interface. Detailed procedure of the LMDS algorithm can be found in section S5 and algorithm S2 in the Supplementary Materials.

Figure 4 shows the comparative analysis between LMDS and typical clustering algorithms. For layered samples, deep layers can lead to large peak positioning errors comparable to layer interval; in other words, interclass distance and intraclass distance may fall in a similar order of magnitude. In this case, K-means clustering is highly unstable because of its sensitivity to the initial value when the clusters are close to each other (Fig. 4A). Meanwhile, K-means clustering requires prior knowledge of the cluster number that is in practice unknown a priori, and actual layers with some degree of warping blur the cluster center as well.

Density-based spatial clustering of applications with noise (DBSCAN) is a density-based clustering method that defines the cluster as the largest set of connected points (*27*). It performs well

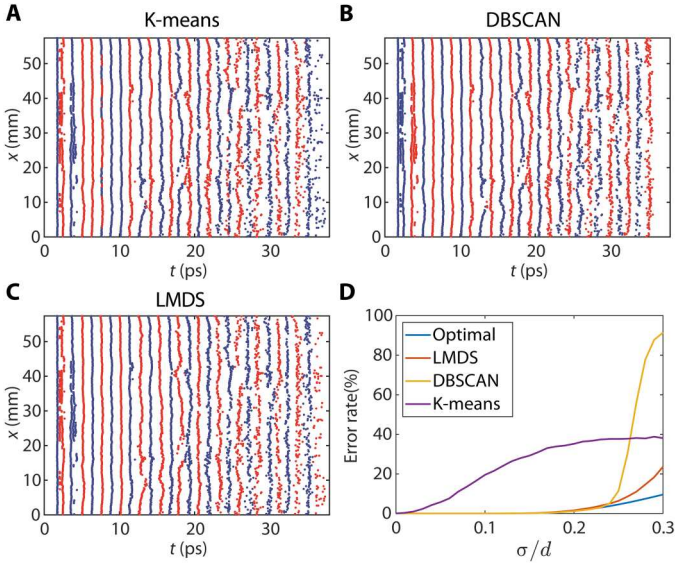

Fig. 4. Comparison of layer segmentation ability of K-means, DBSCAN, and LMDS method. (**A**) K-means initialized with K-means++. The point cloud consists of the first 28 positive peaks extracted by applying the LSPF on measured data. Blue points indicate odd-indexed layers, and red points indicate even-indexed layers. (**B**) DBSCAN. (**C**) LMDS. (**D**) Comparison between various segmentation methods on the simulated data. The location of the simulated point cloud is generated from a Gaussian mixture model with the same SD σ and center distance d of each Gaussian distribution. The optimal boundary is set at the center of the mean of adjacent Gaussian distributions.

in the middle layers but fails at the shallow and deep layers (Fig. 4B). In shallow layers, pulse distortion caused by out-of-focus induces secondary peaks, which are mistakenly identified as directly density-reachable terms and lead to the first two interfaces being marked as the same interface. For the deep layers, the peak point cloud is too sparse to be a core object, hence being ignored. These drawbacks are mainly attributed to the density definition of DBSCAN for being adaptable to high-dimensional data with small distribution deviations. By contrast, the Gaussian density function and local mode in LMDS are capable of suppressing considerable noise and achieve excellent performance with the sample composed of compacted thin layers (Fig. 4C).

Figure 4D provides quantitative comparisons among the above segmentation methods under different point cloud dispersion conditions. The degree of point cloud dispersion is evaluated by the ratio of SD σ to layer interval d. The blue line indicates the error rate of the optimal segmentation boundary. As σ/d increases, K-means clustering quickly fails at the beginning, while DBSCAN and LMDS perform well when the dispersion of the point cloud is not so large. However, the accuracy of DBSCAN breaks down at $\sigma/d = 0.24$ because large deviations change the density-reachable relationship. LMDS method performs quite well even when the relative deviation reaches $\sigma/d = 0.3$. Following the peak finding of pulse sequences, layer segmentation assists in the successful extraction of layer interfaces from the point clouds to reconstruct the structure of layered samples.

Layer image acquisition

After the reconstruction of the layer structure, transverse THz images within various layers can be obtained by extracting the amplitude information from corresponding pulses. Ideally, THz images can be obtained by simple amplitude mapping of the peaks of reflected THz signals. However, the quality of deep-layer images is seriously deteriorated by three main factors. First, measurement errors add a layer of random noises to the reflected signal. Second, the peak finding error introduces the amplitude error. Last but not least, multiple reflections generate many small pseudo pulses that are scattered around the original single-reflection pulse, thereby changing the original peak amplitude and pulse shape to cause large oscillation in the image. As the energy of multiple reflections reaches a single reflection in deep layers, the image contrast drops drastically and becomes unrecognizable.

Fortunately, the random distribution of multiple-reflection pulses only changes the amplitude of every single point, while the integral of the pulse remains unchanged because of the linear superposition nature of the signal. Therefore, pulse integration can remove the randomness of multiple-reflection distribution in each layer. In this case, we propose an average-amplitude THz imaging, named pulse neighborhood average imaging (PNAI) method, to obtain high-contrast THz images from structures with dozens of layers.

PNAI uses the average value of the interval around the peak for imaging, which also suppresses random noise and peak finding error (see section S6 for details). To determine the appropriate average interval, we introduce image kurtosis as a way to balance the SNR and overlap to search for the highest image contrast corresponding to optimal interval length (see section S7 for details). After acquiring average values of all pulses, PNAI calculates the difference between positive and negative pulses to eliminate systematic errors caused by long-term drift to improve the consistency of the background region. The detailed implementation of the PNAI algorithm can be found in section S7 and algorithm S3 in the Supplementary Materials.

Figure 5A compares PNAI with other robust THz imaging methods. Local peak-to-peak imaging (LPTP) is the most frequently used imaging method for the THz time-domain signal that uses the local extremum as the representative of pulse amplitude. However, multiple reflections introduce notable oscillation in the images, which gradually overshadows the attenuated content and makes the image nearly unrecognizable. Time-gated spectral imaging (TGSI) considers different frequency response of layers and selects the optimal frequency component to improve the image contrast (*18*), which has a better performance than LPTP. However, TGSI is extremely sensitive to both the position and the length of the time slice. For instance, peak finding error leads to complete failure of TGSI for the letter "W". Moreover, the time-gated Fourier transform can perform reasonably well in the first few layers, but the spectrum is markedly disturbed in deep layers by multiple reflections, pulse overlap, and out-of-focus.

PNAI uses the exact peak positions at different points to avoid the unwanted content superposition caused by the warping of deep layers ("T", "W", and "X"). Even if the peak finding error is considerably large, the average process will reduce the amplitude deviation and maintain the consistency of images, making it suitable for thin warping layers. Moreover, the contrast enhancement of the averaging process is substantial. As shown in Fig. 5B, more averaging points lead to a better suppression effect on the stochastic noise and multiple reflections and improves the consistency of the background region, while aggravating unfavorable pulse overlap as shown by the negative image of the letter "Y" in the right panel. The middle panel in Fig. 5B has the highest kurtosis, corresponding to high contrast as well as minor overlap.

It is worth noting that several characters from other layers also appear in the image (Fig. 5A). For example, "F" appears in the image of layer 7, and "U" and "V" appear in the image of layer 20. This superposition creates strong ambiguity for content recognition

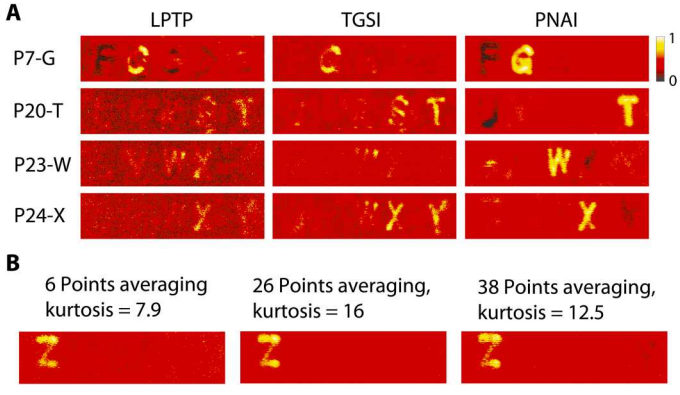

Fig. 5. Performance of the imaging methods. (**A**) Comparison between three robust imaging algorithms: PNAI, local peak-to-peak imaging (LPTP), as well as time-gated spectral imaging (TGSI). Locations of the layers are provided by our proposed layer-structure reconstruction method. The color bar indicates the normalized field amplitude at time domain for PNAI and LPTP and the average of contrasting spectral component amplitude in TGSI in arbitrary units. (**B**) Imaging result of letter Z with various interval lengths.

and seriously degrades the image quality. In most cases, the shadow and pulse overlap can be regarded as a linear superposition of adjacent layers. Therefore, their effect can be eliminated by a reverse superposition process once the superposition coefficient is known. For sample structures of a binary or ternary nature, it is possible to determine the superposition coefficient from the image statistics rather than the physical model. Consequently, we propose a moment maximization method by introducing higher-order statistics to represent the essence of data distribution.

For noiseless binary images with discrete statistics, the normalized even-order central moments can be expressed by

$$M(X) = \frac{\sum_{i=1}^{3} p_i [x_i - E(X)]^{2r}}{D(X)^r}, \quad \text{where} \quad E(X) = \sum_{i=1}^{3} p_i x_i;$$

$D(X) = \sum_{i=1}^{3} p_i [x_i - E(X)]^2$; x_1, x_2, and x_3 represent the amplitude of the content region, superposition region, and background region respectively; p_1, p_2, and p_3 represent the region proportion respectively; $2r$ represents the order. The amplitude of the superposition region x_2, as an independent variable, gradually changes during the reverse superposition process. M reaches a local maximum when x_2 is equal to x_3, which means that the image superposition is fully compensated (see section S8 for details). Actual images are influenced by noise, mostly Gaussian, which transforms the statistics of the image into a continuous form. Although the extremum condition of the discrete image may be no longer valid, the coefficient error can be ignored when the SD of the noise is less than half of the content amplitude, and the residual superposition becomes nearly unrecognizable. Detailed procedure of the moment maximization algorithm is described in section S8 and algorithm S4 in the Supplementary Materials.

Figure 6 reveals the performance of the moment maximization algorithm for superposition elimination. The superimposed characters in layers 4 and 7 mainly originate from the shadow of the preceding layer, while those in layers 13 and 15 are mainly from the overlap with the subsequent layer. Simple thresholding performs poorly because the amplitude of the superposition region is close to the background. Our moment maximization method successfully eliminates the unhelpful superpositions, and the quality of the resulting THz images is comparable with optical images of the letter on single sheets of paper.

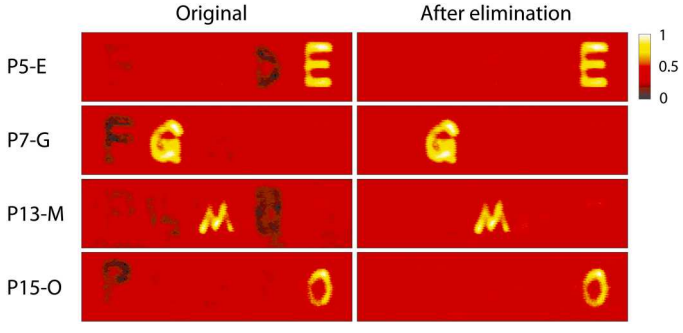

Fig. 6. Performance of moment maximization algorithm. The left column shows the original images, and the right column shows images after the superposition elimination. Images are normalized separately with the mean value set to 0.4.

After applying all the techniques mentioned above, THz images of all the layers are successfully obtained with excellent consistency and image quality as shown in Fig. 7A. The high contrast of the last few sheets demonstrates that 26 layers do not reach the layer limit of our method, while it is restricted by the range of optical delay line of our THz-TDS system. Figure 7B shows the estimated SNR of THz signals for each layer. Paper has a lower reflectivity than ink, hence the lower SNR. The SNR of paper drops quickly in the first dozen layers and then oscillates around −6 dB, which is consistent with the multiple-reflection model. It also demonstrates that LSPF enables accurate structure reconstruction even at SNR as low as −6 dB, which outperforms conventional algorithms (fail after layer 16) by at least 10 dB. Figure 7C uses the peak SNR (PSNR) to evaluate the quality of THz images obtained by various imaging algorithms. LPTP has a poor performance because the peak-to-peak value amplifies the noise under low SNR, and the warping of deep layers also causes serious superposition. Compared with simple amplitude mapping, the averaging process of PNAI results in a 7 dB enhancement in the average PSNR and provides about 10 dB enhancement for the last few layers, indicating that our proposed imaging method provides a substantial improvement in image contrast.

To further demonstrate the inspection ability of our proposed method, nine words "Xi′an," "Jiaotong," "University," "Liuyang," "Zhang," "Terahertz," "Inspection," "Research," and "Group" are written on the odd-indexed layers from layer 3 to 19 of the 22-layer paper stack. THz images of corresponding layers are shown in Fig. 8, with all the words clearly recognizable.

Applications in cultural heritages

Cultural artifacts, such as murals or canvas paintings, may also be featured with layered structures due to the creation and restoration processes. Our proposed method can inspect the layered structure, internal defects, and hidden paint layers of the artworks and provide internal information about the creation technique and the deterioration process. For example, the Emperor Qin Shi Huang Mausoleum in Xi′an has unearthed around 8000 Terra-Cotta Warriors, most of which are lavishly painted in a range of vibrant colors including green, purple, red, and blue. The life-size Terra-Cotta Warriors are displayed in the Mausoleum Site Museum in Fig. 9A. Since the excavation, however, the Terra-Cotta Warriors have been exposed to a much less humid environment, causing the paint layers to shrink, crack, and flake off the terra-cotta surface. Therefore, the structure and aging condition of the paint layers needs to be examined to protect and repair the warrior at an early stage. As shown in Fig. 9B, our proposed method can properly visualize the top and bottom surfaces of the paint layer on a warrior fragment. The refractive index of the pigment in the THz region is measured to be n = 2.9, and the average thickness of the paint layer can be known to be 140 μm. Two detected interfaces show that the paint layer on the sample was painted at the same time. Once the layered structure is determined, THz images at each interface can be obtained. Figure 9C shows the THz image of the bottom surface, which is the interface between the pigment and the clay. Because the reflection of THz waves between pigment and air is much stronger than that between the pigment and clay, the amplitude of the THz image can indicate the severity of the pigment detachment. As shown in Fig. 9C, three areas at the edge of the sample are measured with an

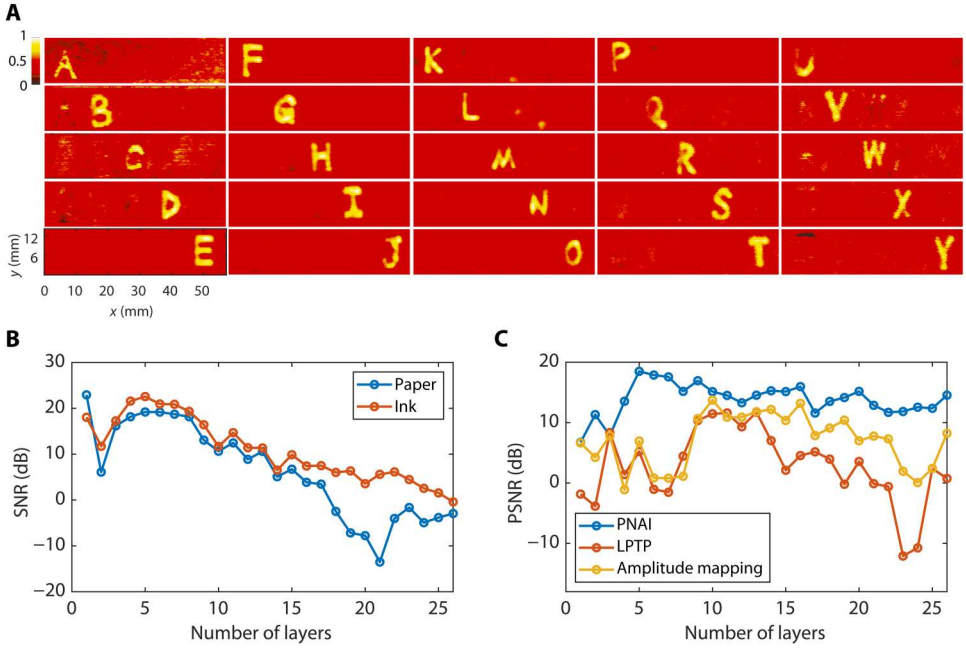

Fig. 7. Evaluation of THz imaging results. (**A**) THz images of each layer. The proposed method successfully obtained layer images with high contrast and consistency. The image of the last page with the letter "Z" can be found in Fig. 5B. Images are normalized separately with the mean value set to 0.4. (**B**) Estimated SNR of THz signals for each layer. SNR is defined as $20\log_{10}(A_s/A_n)$. The signal amplitude A_s is calculated from half of the difference between adjacent positive and negative peaks, and the noise amplitude A_n is calculated from the SD of the nine-point neighborhood around the peak. (**C**) Evaluation of the THz image quality using the peak SNR (PSNR). PSNR is calculated from the normalized mean square error between the THz image and the binarized optical image (reference).

optical microscope, the rightmost two of which correspond to high-amplitude regions in the THz image. The result shows that high-amplitude regions in the THz image of the underside indicate the presence of pores and debonding under the paint layer, which provides a nondestructive inspection method for assessing the deterioration of the paint layers in Terra-Cotta Warriors. Early conservation can then be achieved by reinforcing large debonding areas with a 5% polyacrylate binder.

To further demonstrate the applicability of our method to the multilayer painted samples, we prepare a nine-layer test sample using ochre and yellow ochre pigments bound with gelatin. To prepare the sample, ochre pigments are first applied evenly to a glass substrate. After drying for 20 min, another layer of ochre is painted over the dried pigment, and the painting process is repeated eight times. After each even-indexed layer of ochre has been applied, one letter of "X," "J," "T," and "U" is painted with the yellow ochre pigment. Figure 10A shows the stratigraphic reconstruction and imaging of the testing sample by our proposed method. Reflection interfaces of THz pulses are formed between the pigments dried at different times, and therefore, the extracted peak point cloud indicates the position of the paint layers. As shown in the top right inset in Fig. 10A, the local maxima marked by the red dots in the density function correspond to the interface positions, and the segmentation boundaries can be set in the middle of adjacent interfaces. As shown in the bottom plot, the hidden characters painted on the corresponding layers can be clearly recognized. Figure 10B shows the formation of internal defects in the multilayer painted sample after 6 months of exposure to the atmosphere. In addition to the interface between the pigment layers, the cracks and debonding also appear as highly reflective interfaces of the THz pulses that can be identified

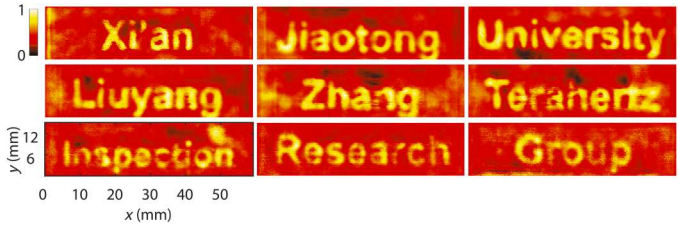

Fig. 8. THz imaging of a document. The sample consists of 22 paper sheets, and nine words are written on the odd-indexed layers. Materials are the same as the 30-layer sample. Images are normalized separately with the mean value set to 0.4.

by the LSPF algorithm. The position of cross-layer cracks and debonding between layer 9 and the substrate is shown in the top plot of Fig. 10B, with two cracks propagating through layers 4 to 5 and layers 6 to 8, respectively. The bottom plot shows the THz image obtained at the defect positions, and the image amplitude indicates the severity of the cracks and debonding. It can be concluded that our proposed method successfully inspects the structure, internal defects, as well as hidden content in the layered artworks, which shows its large potential to evaluate the deterioration process and extract the hidden information for layered cultural heritage.

DISCUSSION

Multiple reflections play the dominant role in the inspection of layered structures that has been seldom investigated by previous work. The multiple-reflection model reveals that the SNR is highly dependent on the layer numbers. For structures with dozens of layers, the energy attributed to multiple reflections

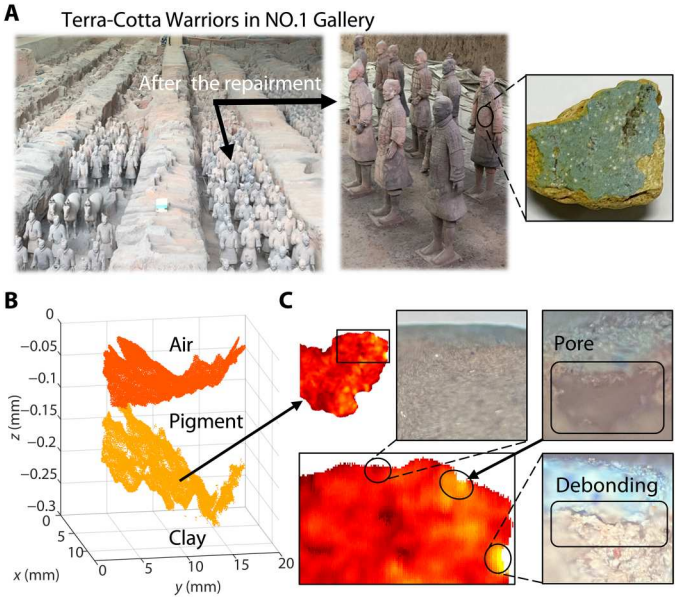

Fig. 9. Application to the Terra-Cotta Warriors. (**A**) Excavated Terra-Cotta Army and conservation of life-sized warriors. (**B**) Structure reconstruction and thickness measurement of warrior fragments. (**C**) THz imaging of the bottom surface. High-amplitude regions in the THz image indicate pores or debonding.

oscillates around a single reflection, and the SNR drops below one regardless of the measurement system. This may be counterintuitive because it is commonly believed that the penetration depth of the layered structure is determined by the THz source power. However, as multiple reflections are also proportional to the emitted pulse, the noise induced by irregular multiple reflections increases at the same rate as a single reflection. Therefore, robust peak finding and imaging algorithms become rather important for layered structures.

In this work, inspired by the notable oscillation of reflected THz signals from layered structures, we use the local symmetrical feature of THz pulses rather than their amplitude, derivative, or shape for the pulse position extraction, which enables accurate peak finding at SNR as low as −6 dB and outperforms conventional algorithms by at least 10 dB. The oscillation of THz signals also results in noticeable noise in the peak point cloud. Therefore, we use the point cloud density defined by the Gaussian function to robustly execute layer segmentation. It is worth noting that the distribution of multiple-reflection pulses can be roughly predicted after the reconstruction of former layers, which might be helpful to filter this kind of noise. Removal of such noise based on the multiple-reflection model can be another topic of further study.

Subsequently, the PNAI method also fully considers multiple reflections to eliminate the noise caused by randomly distributed pulses through averaging process, and the average PSNR increases by approximately 7 dB in our experimental setup. PNAI may aggravate overlap when the pulse interval is considerably small. However, the unwanted content superposition can be mostly eliminated through the moment maximization method. The idea of average imaging can be easily extended to other time-domain imaging techniques. For example, LPTP could use the average value around local extrema instead of single-point amplitude to enhance the contrast of THz images.

Last, the experiment demonstrates that our proposed framework can extract hidden structural and content information from subwavelength layered paper with high resolution and contrast, which has great potential for the detection of ancient documents. The method also performs layer reconstruction and debonding inspection in the conservation of Terra-Cotta Warriors and provides a new approach to study the internal information of multilayer painted samples. The proposed peak finding and imaging method provide fine image quality. This work provides practical solutions for THz-TDS to inspect conventional layered structures with submillimeter thicknesses and can be efficiently extended to other pulse imaging techniques.

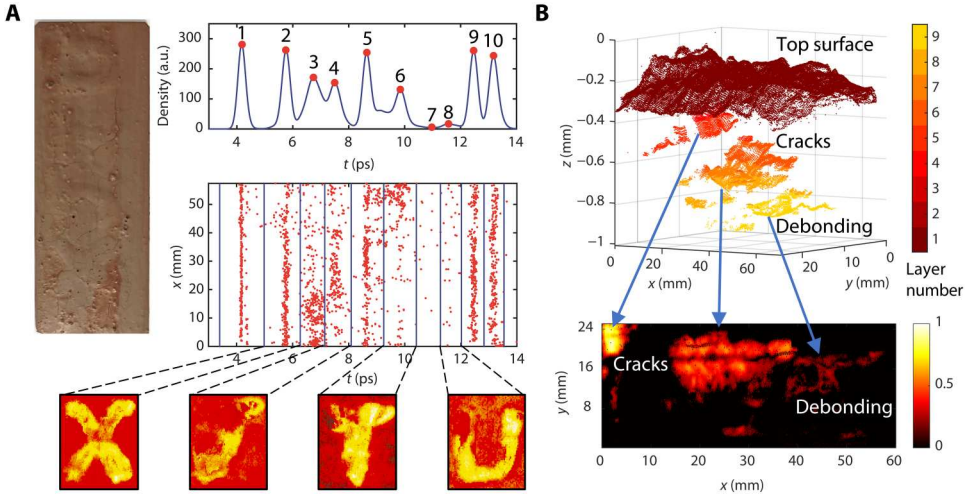

Fig. 10. Application to multilayer painted samples. (**A**) Stratigraphic reconstruction and imaging of a nine-layer painted sample. Hidden characters painted on the corresponding layers can be recognized. (**B**) Inspection of debonding and cross-layer cracks in the multilayer painted sample after 6-month aging. The bottom image shows the relative severity of the cracks and debonding of the sample.

MATERIALS AND METHODS

THz-TDS system specification

The data are collected using Teraview's THz-TDS in the ambient atmosphere. The measurement system has a bandwidth of 4 THz with a center frequency of 1 THz. The time delay range of the mechanical delay line is up to 51 ps, and the time resolution is 23 fs. The system uses photoconductive antennas pumped by a femtosecond laser at 80-MHz repetition rate for the generation and detection of THz waves with a dynamic range of 60 dB. The THz waves are focused using lenses with a focal length of 18 mm. The acquisition rate of the system is 15 waveforms per second.

Preparation of the layered sample

The sample consists of 30 layers of compacted plain paper sheets with a thickness of 100 μm, and 26 English alphabetic letters from A to Z are written with a black gel pen on one side of the first 26 sheets, respectively. The THz beam is focused on the middle layer of the sample, with a scan area of 57.5 mm by 14.4 mm and scan steps of 0.2 and 0.25 mm in the x and y axes, respectively.

Signal alignment of the layered sample

After extracting the pulse positions using the LSPF algorithm, the peak point cloud representing the layer structure can be obtained. To improve the 1D divisibility of the point cloud, an alignment strategy is applied to the point cloud and the THz time-domain signal. This strategy aligns the first positive peak of different signals by shifting the signals along the time axis. Figures 3 and 4 show the B-scan and point cloud after the alignment.

Supplementary Materials

This PDF file includes:

Sections S1 to S8
Figs. S1 to S6
Algorithm S1 to S4

REFERENCES AND NOTES

1. S. Helal, H. Sarieddeen, H. Dahrouj, T. Y. Al-Naffouri, M. S. Alouini, Signal processing and machine learning techniques for terahertz sensing: An overview. *IEEE Signal Proc. Mag.* **39**, 42–62 (2022).
2. P. U. Jepsen, D. G. Cooke, M. Koch, Terahertz spectroscopy and imaging - Modern techniques and applications. *Laser Photonics Rev.* **5**, 124–166 (2011).
3. D. M. Mittleman, Perspective: Terahertz science and technology. *J. Appl. Phys.* **122**, 230901 (2017).
4. J. Neu, C. A. Schmuttenmaer, Tutorial: An introduction to terahertz time domain spectroscopy (THz-TDS). *J. Appl. Phys.* **124**, 231101 (2018).
5. W. Withayachumnankul, M. Naftaly, Fundamentals of measurement in terahertz time-domain spectroscopy. *J. Infrared Millim. Te.* **35**, 610–637 (2014).
6. R. I. Stantchev, B. Q. Sun, S. M. Hornett, P. A. Hobson, G. M. Gibson, M. J. Padgett, E. Hendry, Noninvasive, near-field terahertz imaging of hidden objects using a single-pixel detector. *Sci. Adv.* **2**, e1600190 (2016).
7. X. Yang, X. Zhao, K. Yang, Y. P. Liu, Y. Liu, W. L. Fu, Y. Luo, Biomedical applications of terahertz spectroscopy and imaging. *Trends Biotechnol.* **34**, 810–824 (2016).
8. J. Dong, J. B. Jackson, M. Melis, D. Giovanacci, G. C. Walker, A. Locquet, J. W. Bowen, D. S. Citrin, Terahertz frequency-wavelet domain deconvolution for stratigraphic and subsurface investigation of art painting. *Opt. Express* **24**, 26972–26985 (2016).
9. C. L. Koch-Dandolo, T. Filtenborg, K. Fukunaga, J. Skou-Hansen, P. U. Jepsen, Reflection terahertz time-domain imaging for analysis of an 18th century neoclassical easel painting. *Appl. Optics* **54**, 5123–5129 (2015).
10. A. Novikova, D. Markl, J. A. Zeitler, T. Rades, C. S. Leopold, A non-destructive method for quality control of the pellet distribution within a MUPS tablet by terahertz pulsed imaging. *Eur. J. Pharm. Sci.* **111**, 549–555 (2018).
11. J. A. Zeitler, P. F. Taday, D. A. Newnham, M. Pepper, K. C. Gordon, T. Rades, Terahertz pulsed spectroscopy and imaging in the pharmaceutical setting - a review. *J. Pharm. Pharmacol.* **59**, 209–223 (2007).
12. S. Krimi, J. Klier, J. Jonuscheit, G. von Freymann, R. Urbansky, R. Beigang, Highly accurate thickness measurement of multi-layered automotive paints using terahertz technology. *Appl. Phys. Lett.* **109**, 021105 (2016).
13. S. Unnikrishnakurup, J. Dash, S. Ray, B. Pesala, K. Balasubramaniam, Nondestructive evaluation of thermal barrier coating thickness degradation using pulsed IR thermography and THz-TDS measurements: A comparative study. *NDT&E Int.* **116**, 102367 (2020).
14. D. D. Zhang, J. J. Ren, J. Gu, L. J. Li, J. Y. Zhang, W. H. Xiong, Y. F. Zhong, T. Y. Zhou, Nondestructive testing of bonding defects in multilayered ceramic matrix composites using THz time domain spectroscopy and imaging. *Compos. Struct.* **251**, 112624 (2020).
15. Y. F. Xu, H. K. Zhou, Y. Q. Cui, X. Y. Wang, D. S. Citrin, L. Y. Zhang, R. Q. Yan, X. F. Chen, Full scale promoted convolution neural network for intelligent terahertz 3D characterization of GFRP delamination. *Compos. Part B Eng.* **242**, 110022 (2022).
16. J. L. Dong, A. Locquet, N. F. Declercq, D. S. Citrin, Polarization-resolved terahertz imaging of intra- and inter-laminar damages in hybrid fiber-reinforced composite laminate subject to low-velocity impact. *Compos. Part B Eng.* **92**, 167–174 (2016).
17. P. K. Lu, D. Turan, M. Jarrahi, High-power terahertz pulse generation from bias-free nanoantennas on graded composition InGaAs structures. *Opt. Express* **30**, 1584–1598 (2022).
18. A. Redo-Sanchez, B. Heshmat, A. Aghasi, S. Naqvi, M. J. Zhang, J. Romberg, R. Raskar, Terahertz time-gated spectral imaging for content extraction through layered structures. *Nat. Commun.* **7**, 12665 (2016).
19. A. Aghasi, B. Heshmat, A. Redo-Sanchez, J. Romberg, R. Raskar, Sweep distortion removal from terahertz images via blind demodulation. *Optica* **3**, 754–762 (2016).
20. Y. F. Xu, X. D. Fang, S. T. Fan, L. Y. Zhang, R. Q. Yan, X. F. Chen, Double Gaussian mixture model-based terahertz wave dispersion compensation method using convex optimization technique. *Mech. Syst. Signal. Pr.* **164**, 108223 (2022).
21. P. Wang, H. Y. Fu, T. Koike-Akino, P. V. Orlik, Multi-layer terahertz imaging of non-overlapping contents. *Pr. IEEE Sen. Array*, 652–656 (2018).
22. J. L. Dong, A. Locquet, D. S. Citrin, Enhanced terahertz imaging of small forced delamination in woven glass fibre-reinforced composites with wavelet de-noising. *J. Infrared Millim. Te.* **37**, 289–301 (2016).
23. L. B. Schafer, U. S. K. P. M. Thanthrige, A. Sezgin, Iteratively reweighted nuclear norm based distortion compensation for THz-TDS, *2022 Fifth International Workshop on Mobile Terahertz Systems (IWMTS)* (2022).
24. Y. F. Xu, H. B. Hao, D. S. Citrin, X. Y. Wang, L. Y. Zhang, X. F. Chen, Three-dimensional nondestructive characterization of delamination in GFRP by terahertz time-of-flight tomography with sparse Bayesian learning-based spectrum-graph integration strategy. *Compos. Part B Eng.* **225**, 109285 (2021).
25. J. A. Grzesik, EM pulse transit across a uniform dielectric slab, *2007 Workshop on Computational Electromagnetics in Time-Domain* (2007), pp. 5–8.
26. P. Bao, L. Zhang, X. L. Wu, Canny edge detection enhancement by scale multiplication. *IEEE T. Pattern Anal.* **27**, 1485–1490 (2005).
27. M. Ester, H. P. Kriegel, J. Sander, X. Xiaowei, A density-based algorithm for discovering clusters in large spatial databases with noise, *KDD-96 Proceedings of the Second International Conference on Knowledge Discovery and Data Mining* (AAAI Press, 1996), pp. 226–231.

Acknowledgments

Funding: This work was supported by the National Natural Science Foundation of China (grant. 52175115). **Author contributions:** L.Z., Y.C., and Y.X. conceived the idea. Y.C. designed the experiment. Y.C. and J.L. prepared the samples. Y.C., Xingyu Wang, Z.S., and Y.H. measured the samples. Y.C. performed the signal analysis and established the model. Y.C. designed all the algorithms and performed the data analysis. Y.C., D.H., and Y.X. performed data visualization. Y.C. wrote the manuscript. Y.C., L.Z., Y.X., Xianqiao Wang, D.S.C., A.K.N., R.Y., and X.C. revised the manuscript. L.Z., R.Y., and X.C. supervised the research. All the authors discussed the results and commented on the manuscript. **Competing interests:** The authors declare that they have no competing interests. **Data and materials availability:** All data needed to evaluate the conclusions in the paper are present in the paper and/or the Supplementary Materials.

Submitted 26 January 2023
Accepted 5 September 2023
Published 4 October 2023
10.1126/sciadv.adg8435